# Improving segmentation accuracy for magnetic resonance imaging using a boosted decision tree

Wen-Hung Chao [a,b], You-Yin Chen [a,*], Chien-Wen Cho [a], Sheng-Huang Lin [c], Yen-Yu I. Shih [d], Siny Tsang [e]

[a] Department of Electrical and Control Engineering, National Chiao Tung University, No. 1001, Ta-Hsueh Road, Hsinchu 300, Taiwan, ROC
[b] Department of Biomedical Engineering, Yuanpei University, No. 306, Yuanpei Street, Hsinchu 300, Taiwan, ROC
[c] Department of Neurology, Buddhist Tzu Chi General Hospital, No. 707, Section 3, Chung Yang Road, Hualien 970, Taiwan, ROC
[d] Institute of Biomedical Sciences, Academia Sinica, No. 128, Section 2, Academia Road, Taipei 115, Taiwan, ROC
[e] Department of Psychology, National Taiwan University, No. 1, Section 4, Roosevelt Road, Taipei 106, Taiwan, ROC

## ARTICLE INFO

## ABSTRACT

The purpose of this study was to improve the accuracy rate of brain tissue classification in magnetic resonance (MR) imaging using a boosted decision tree segmentation algorithm. Herein, we examined simulated phantom MR (SPMR) images, simulated brain MR (SBMR) images, and a real data. The accuracy rate and $k$ index when classifying brain tissues as gray matter (GM), white matter (WM), or cerebral-spinal fluid (CSF) were better when using the boosted decision tree algorithm combined with a fuzzy threshold than when using a statistical region-growing (SRG) algorithm [Wolf I, Vetter M, Wegner I, Böttger T, Nolden M, Schöbinger M, et al. The medical imaging interaction toolkit. Med Imag Anal 2005;9:594–604] and an adaptive segmentation (AS) algorithm [Wells WM, Grimson WEL, Kikinis R, Jolesz FA. Adaptive segmentation of MRI data. IEEE Trans Med Imag 1996;15:429–42]. The segmentation performance when using this algorithm on real data from brain MR images was also better than those of SRG and AS algorithm. Segmentation of a real data using the boosted decision tree produced particularly clear brain MR imaging and permitted more accurate brain tissue segmentation. In conclusion, a decision tree with appropriate boost trials successfully improved the accuracy rate of MR brain tissue segmentation.

Crown Copyright © 2008 Published by Elsevier B.V. All rights reserved.

## 1. Introduction

Magnetic resonance (MR) image segmentation is an important image post-processing for medical research and clinical diagnoses. Brain MR image segmentation is critical to the assessment of brain tissues and neurological disorders, such as Alzheimer's disease and tumors (Rettmann et al., 2002; Anbeek et al., 2004; Zoroofi et al., 2004; Liu et al., 2005; Mohr et al., 2004; Admiraal-Behloul et al., 2005; Gu et al., 2005; Dou et al., 2007; Behrens et al., 2007; Xia et al., 2007). Zoroofi et al. (2004) demonstrated favorable segmentation performance using an automatic segmentation technique combined with region growing, gray morphological dilation, filtering, and thresholding to assess the necrotic formal head area. Admiraal-Behloul et al. (2005) used a fully automatic segmentation method combined with adaptive and reasoning levels to perform white matter hyperintensity (WMH) segmentation for volume qualification and similarity on older MR images. Dou et al. (2007) proposed a

framework of fuzzy information fusion combined with registration operation, feature extraction, fuzzy feature fusion operation, and fuzzy region growing to automatically segment brain tumor tissues on MR images. Xia et al. (2007) proposed a knowledge-driven algorithm for automatically delineating the caudate nucleus (CN) region in MR-imaged human brains. These studies demonstrate the importance of segmentation for neurological applications. In basic segmentation applications, conventional MR image segmentation is used to detect regions of growth and edges (Cline et al., 1987; Joliot and Majoyer, 1993; Schiemann et al., 1996). In the brain, MR image tissue segmentation is important to accurately distinguish gray matter (GM), white matter (WM), and cerebral-spinal fluid (CSF) (Zhou et al., 2001; Andersen et al., 2002; Marroquin et al., 2002; Amato et al., 2003; Gu et al., 2005), while automatic MR image segmentation is often used to classify brain tissue. Many automatic segmentation techniques use probabilistic classification to segment brain tissue (Andersen et al., 2002; Anbeek et al., 2005; Greenspan et al., 2006), while others use wavelet coefficients as spatial features of voxels in three-dimensional (3D) imaging for clustering the GM, WM, and CSF with fuzzy theory. Fuzzy logical models have been used to test phantom, normal, and Alzheimer's

* Corresponding author. Tel.: +886 3 571 2121x54427; fax: +886 3 612 5059.
E-mail address: irradiance@so-net.net.tw (Y.-Y. Chen).

brain MR images in order to reduce the difference of partial volume averaging on the boundary of the ventricles (Barra and Boire, 2000). Another wavelet application has been used to design attribute vectors as spatial features of voxels for determining correspondence in 3D brain MR images (Xue et al., 2004). Segmentation applications include tissue volume quantification and 3D spatial structure reconstruction, which greatly aid in disease diagnosis (Joliot and Majoyer, 1993; Tang et al., 2000; Yoo et al., 2001; Zoroofi et al., 2001, 2004; Archibald et al., 2003; Mohr et al., 2004; Ali et al., 2005; Andrey and Maurin, 2005; He et al., 2005; Shan et al., 2005; Noulhiane et al., 2006).

Several factors make brain MR image segmentation difficult, including similar imaging intensities in different regions of the brain, overlapping intensity distributions, background noise, and radio-frequency (RF) heterogeneities. These factors often affect the accuracy rate. Therefore, many studies have focused on improving the accuracy of MR image segmentation. Marroquin et al. (2002) reported an accurate and efficient Bayesian method for segmenting tissues in brain MR images, and evaluated the performance of this method using quantitative indices for GM and WM on simulated brain MR data. Archibald et al. (2003) improved human brain tissue segmentation in MR images using segmentation preprocessing based on the Gegenbauer reconstruction method. Another method was recently proposed using k-nearest neighbor (KNN) analysis. Here, a feature space is built from spatial information and then applied to the KNN model, which is then used to classify different brain structures. Similar indices (SI) and probabilistic SI (PSI) were measured to evaluate segmentation performance. Segmentation accuracies in which SI values exceeded 0.8 and PSI values exceeded 0.7 for all tissues indicated good agreements (Anbeek et al., 2004, 2005). RF inhomogeneity correction has also been used as a preprocessing method to improve image segmentation (Zhou et al., 2001; Andersen et al., 2002). Most of these techniques are automatic and, therefore, efficient; however their applications are sometimes limited to GM and WM delineation, while their accuracy has room for improvement. To address these problems, we propose the use of decision trees as an easier way to segment brain MR images.

Decision trees can be constructed from many specific algorithms. A classification and regression tree (CART) can be applied for classification analysis while also acting as a regression tree. CART is a binary tree that has been utilized in many studies (Grajski et al., 1986; Bittencourt and Clarke, 2003; Hautaniemi et al., 2005). The C4.5 learning method proposed by Quinlan (1993) is another decision tree that was reformed from the ID3 learning system proposed by Quinlan (1986) and used in a supervised classification problem. The C4.5 was advanced to the See5/C5.0 to improve decision tree performance (Quinlan, 1996, 2003). The ID3, C4.5, and C5.0 have been used for classification in many studies. The C4.5 learning system was used to determine the optimal subset of a control system for selecting attributes among continuous attributes, noise data, and alternative measures (Shiue and Guh, 2006). The C5.0 was used to classify electrocardiograms (ECG) in a healthy control subject and in a subject with a heart disorder, wherein three experiments were conducted including classifications based on 2, 3, and 7 classes. This system was successfully used to classify bundle branch block, cardiomyopathy, arrhythmia, healthy control, hypertrophy, myocarditis, and myocardial infraction with good accuracy (Macek, 2005). We used a decision tree in our study because it has several advantages in biomedical applications. Specifically, it can be effectively used to classify any data structure, it can perform with good prediction accuracy for non-linear problems, it is easy to interpret rules in a rule set of the decision tree, and it effectively eliminates outliers (Hautaniemi et al., 2005). Therefore, we propose a boosted decision tree algorithm combined with fuzzy threshold for the classification of brain tissues, such as GM, WM, and CSF, with the goal of improving accuracy rates of brain MR image segmentation.

The rest of this paper is organized as follows: Section 2 presents materials and methods including MR data acquirement, image pre-processing, and details of segmentation algorithm with the boosted decision tree. Section 3 shows the results of segmentation using the boosted decision tree and other methods from MR data. The discussions of this study and comparison with other methods are shown in Section 4. Finally, the conclusions of this present study are shown in Section 5.

## 2. Materials and methods

### 2.1. MR data

Two types of simulated data were used in this study, including simulated phantom MR (SPMR) images and simulated brain MR (SBMR) images. The SPMR images were obtained from IBSR (http://www.cma.mgh.harvard.edu/ibsr). The SPMR images consisted of a circle center, circle ring, and background region, with noise variations of 15 or 30 gray levels. RF heterogeneities of 20% and 40% were also combined in the two SNRP images. The gray level variation due to noise and the heterogeneities added to a phantom image is summarized in Table 1. The simulated brain MR images obtained from BrainWeb (http://www.bic.mni.mcgill.ca/brainweb) were T1-weighted images with resolutions of $256 \times 256 \times 181$ voxels, with $1\,\text{mm} \times 1\,\text{mm} \times 1\,\text{mm}$ voxel dimensions. The simulated BrainWeb images were provided with their ground truth and the noise levels (3%, 5%, 7%, and 9%), inhomogeneity of the simulated brain images can also be controlled. Furthermore, RF heterogeneities of either 20% or 40% were added to the images, with noise level respectively described in Table 2. These images provided the ability to examine performance with spatial information of varying quality. An expert manually labeled an exemplar brain MR image from the original image with no noise and heterogeneities; this was used as our standard image. All of the simulated data were preprocessed to obtain spatial features and then segmented using the decision tree algorithm.

**Table 1**
Designations of original phantom images obtained by combining noise levels and heterogeneities

| Designation | Noise level and heterogeneity parameters |
| --- | --- |
| Var15 | Noise variation = 15 gray levels |
| Var30 | Noise variation = 30 gray levels |
| Var15RF20 | Noise variation = 15 gray levels and 20% RF heterogeneity |
| Var30RF20 | Noise variation = 30 gray levels and 20% RF heterogeneity |
| Var15RF40 | Noise variation = 15 gray levels and 40% RF heterogeneity |
| Var30RF40 | Noise variation = 30 gray levels and 40% RF heterogeneity |

**Table 2**
Designations of original simulated MR images (BrainWeb) obtained by combining the noise levels and heterogeneities

| Designation | Noise level and heterogeneity parameters |
| --- | --- |
| T1n3 | Noise level = 3% |
| T1n5 | Noise level = 5% |
| T1n7 | Noise level = 7% |
| T1n9 | Noise level = 9% |
| T1n3RF20 | Noise level = 3% and 20% RF heterogeneity |
| T1n5RF20 | Noise level = 5% and 20% RF heterogeneity |
| T1n7RF20 | Noise level = 7% and 20% RF heterogeneity |
| T1n9RF20 | Noise level = 9% and 20% RF heterogeneity |
| T1n3RF40 | Noise level = 3% and 40% RF heterogeneity |
| T1n5RF40 | Noise level = 5% and 40% RF heterogeneity |
| T1n7RF40 | Noise level = 7% and 40% RF heterogeneity |
| T1n9RF40 | Noise level = 9% and 40% RF heterogeneity |

Real data of brain MR images were also used for this experiment. Healthy participants were scanned with a 1.5T MRI system (Signa NV/i, GE Medical Systems, Waukesha, WI) in Buddhist Tzu Chi General Hospital using a standard head coil and an adjustable padded head holder to minimize head motion. The 3D T1-weighted time-of-flight fast spoiled gradient recalled acquisition in steady state (FSPGR, TR/TE = 13.4/2.7 ms, NEX = 1, FOV = 260 mm; 512 × 256 matrix, slice thickness = 2 mm) pulse sequence was used. 144 axial slices were acquired encompassing the whole brain.

## 2.2. Image preprocessing

Spatial features were extracted from every MR image pixel location and used as the input for the segmentation algorithm for image preprocessing. The spatial features used in the present study were: $G$, $S$, $W$, $x$, $y$, $r$, and $\theta$, where $G$ represents the gray level intensity of every pixel, $S$ is the spatial gray level of every pixel, $W$ is the coefficients of the wavelet transform, $(x,y)$ Euclidean coordinates, and $(r,\theta)$ polar coordinates. The spatial features of the general gray level, spatial gray level, and wavelet transform were combined in Euclidean coordinates $(x,y)$ or polar coordinates $(r,\theta)$ by image preprocessing. Noise and RF heterogeneities often reduced the quality of MR images, such that their impact on segmentation accuracy needed to be reduced by image manipulation.

The general gray level represents the intensity of each pixel for MR image segmentation. The use of more spatial features in an image is considered to improve the accuracy of image segmentation. The spatial gray ($S$) level is given as

$$S(x, y) = \sum_{i=1}^{n} \omega_i g_i(x, y) \tag{1}$$

which is the sum of combined weighting $\omega_i$ and gray level $g_i(x,y)$ of pixel $i$ on the neighboring area. The neighboring area is shown in Fig. 1(a), which depicts the five neighbor systems used in this study, wherein the gray level weighting at the center pixel with the nearest four pixels produced $n = 5$ and $\omega_i = 1/5$.

The wavelet transform ($W$) of the spatial features used in this study was the coefficient of the wavelet transform transferred from nine gray levels of each local area to represent the wavelet spatial features of the center pixel for every location. The scaled and translated basis functions are defined as

$$\varphi_{j,m,n}(x, y) = 2^{j/2}\varphi(2^j x - m, 2^j y - n), \tag{2}$$

$$\psi_{j,m,n}(x, y) = 2^{j/2}\psi(2^j x - m, 2^j y - n), \quad i = \{H, V, D\}, \tag{3}$$

where the index $i$ identifies the directional wavelets in $\psi^H(x,y) = \psi^H(x)\varphi(y)$, $\psi^V(x,y) = \varphi(x)\psi(y)$, and $\psi^D(x,y) = \psi(x)\psi(y)$. The discrete wavelet transform of function $g(x, y)$ of size $M \times N$ is then

$$W_\varphi(j_0, m, n) = \frac{1}{\sqrt{MN}} \sum_{x=0}^{M-1}\sum_{y=0}^{N-1} g(x, y)\varphi_{j_0,m,n}(x, y), \tag{4}$$

$$W_\psi^i(j_0, m, n) = \frac{1}{\sqrt{MN}} \sum_{x=0}^{M-1}\sum_{y=0}^{N-1} g(x, y)\psi_{j,m,n}^i(x, y), \quad i = \{H, V, D\}, \tag{5}$$

where the $W_\varphi(j_0,m,n)$ coefficients define an approximation of $g(x,y)$ at scale $j_0$. The $W_\psi^i(j_0, m, n)$ coefficients add horizontal, vertical, and diagonal details for scales $j \geq j_0$ (Gonzalez and Woods, 2002). The obtained coefficients were transferred by wavelet from the local area to represent the spatial features of the central pixel. Local areas were generated from every nine pixels in each MR image, as shown in Fig. 1(b).

## 2.3. Segmentation

A decision tree combined with boost trials and a fuzzy threshold was used in this study. This method was shown by Quinlan to model the prediction tree using a statistical analysis that considered outcome variables to make an accurate prediction (Quinlan, 2003). The image segmentation processing procedures are summarized in Fig. 3. A standard image was trained using the boosted decision tree with a fuzzy threshold, while images with noise levels and RF heterogeneities were then tested by the decision tree constructed from the trained structures. The operation is described as follows.

### 2.3.1. Decision tree classification

The decision tree builds a classifier form that can be integrated using boosting and a fuzzy threshold (Quinlan, 1993, 2003; Dombi and Zsiros, 2005). Regions and tissues in the SPMR images were divided into three and four classes of the decision tree, respectively. A schematic diagram of the decision tree structure is shown in Fig. 2. A decision tree is a tree structure that grows from a root node, flows outward toward internal nodes, and terminates at leaf nodes. The leaf nodes represent the class, wherein the classifier is a model derived from the training dataset and is applied to predict class values in a test dataset. In the tree structure, each internal node is divided by a condition related to a feature, and each branch denotes the outcome of attribute splitting. Each node (root node and internal node) is split into two or more branch nodes. Examples of splitting conditions include "A > a," "B > b," or "C > c" for each node in every attribute, as shown in Fig. 2. Branch splitting is determined by the condition of each node. The leaf nodes depict classification by these splitting conditions, and the class is labeled on the leaf
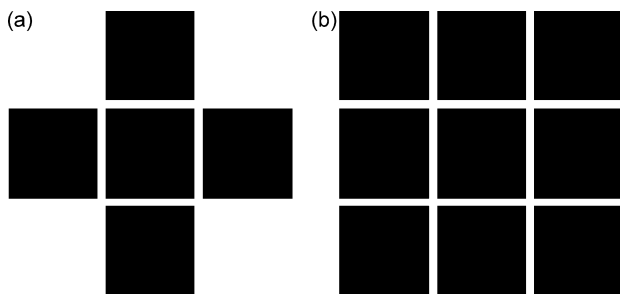


**Fig. 1.** Local area of each spatial feature. (a) Local area of the spatial gray level. (b) Local area of the wavelet transform.
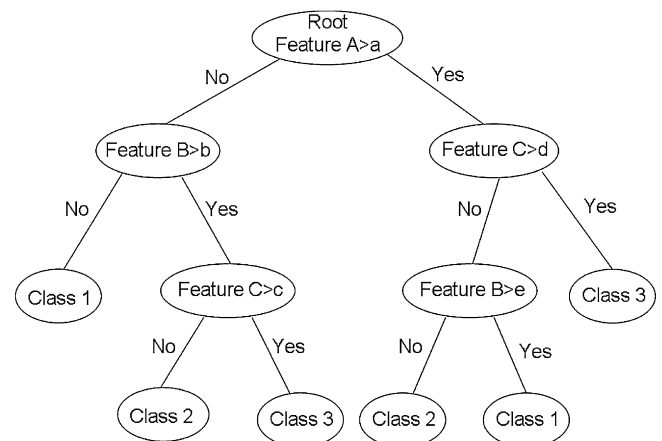


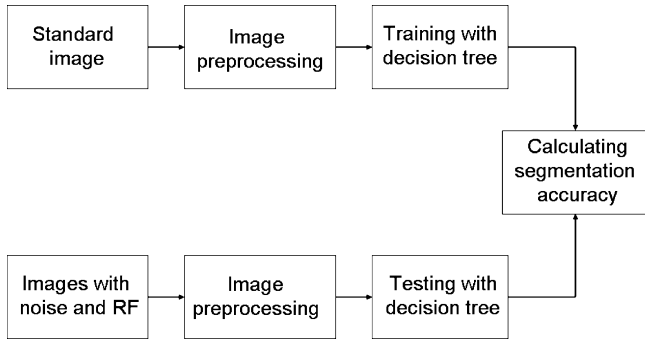**Fig. 2.** Schematic diagram of the decision tree structure.

**Fig. 3.** A flow diagram of image processing procedures for MR image segmentation.

node. The decision tree structure can be transferred into a set of rules.

### 2.3.2. Decision tree construction with gain ratio

The proposed decision tree is constructed from a data set $S$ by the training criteria, Gain Ratio, which is a measure of incorporated entropy (Quinlan, 1993; Frey and Fisher, 2003; Ranilla et al., 2003; Dombi and Zsiros, 2005; Hu et al., 2007). The procedures of Gain Ratio are defined as follows. For simulated MR data, assume that a training data set $S$ consists of $C$ class examples. The function $p(S,r)$ is the ratio for the class number of an MR data set belonging to class $r$ of the total class number $|S|$ of an MR data set $S$, where $1 \leq r \leq C$. The entropy is defined as

$$\text{Entropy}(S) = -\sum_{r=1}^{C} p(S,r)\log_2 p(S,r). \tag{6}$$

Suppose that $T$ is a feature whose total partitions are $v$. The value $i$ is any specific value of $v$, while $S_i$ is a subset of the MR data set $S$ corresponding to the value $i$ of $T$. The information gain, $\text{Gain}(S,T)$, corresponding to the partitioning of $S$ from feature $T$, is calculated by:

$$\text{Gain}(S,T) = \text{Entropy}(S) - \sum_{i=1}^{v} \frac{|S_i|}{|S|}\text{Entropy}(S_i), \tag{7}$$

where $|S_i|$ is the number of subsets $S_i$ in the MR data, and $\text{Entropy}(S_i)$ is calculated similarly as $\text{Entropy}(S)$. In order to obtain a good generation by reducing bias, the gain ratio $\text{GainRatio}(S,T)$ was calculated, wherein the SplitInfo (Eq. (8)) is first provided as:

$$\text{SplitInfo}(S,T) = -\sum_{i=1}^{v} \frac{|S_i|}{|S|}\log_2\left(\frac{|S_i|}{|S|}\right). \tag{8}$$

The function $Gain(S,T)$ is very sensitive to the value of $v$, so the ratio of information gain is calculated as:

$$\text{Gain Ratio}(S,T) = \frac{\text{Gain}(S,T)}{\text{SplitInfo}(S,T)}. \tag{9}$$

The feature $T$ satisfies:

$$\Gamma = \arg\max_{T}(\text{GainRatio}(S,T)) \tag{10}$$

and is selected as the reference for this step of partitioning. The decision tree is constructed by splitting all of the features and maximizing the gain ratio ($\Gamma$).

### 2.3.3. Boosting

The addition of boosting to a decision tree as a means to improve prediction accuracy is know as adaptive boosting, and was proposed by Freund and Schapire (1996, 1999; Quinlan, 1993, 2003; Arditi and Pulket, 2005). Adaptive boosting is based on a learning algorithm of a decision tree classifier over a repeated series of trials: $t = 1, \ldots, T$. One possible approach is to select a best weight and tree structure from the distribution of weights over the training set.

For a training set $(x_i, y_i)\ldots(x_m, y_m)$, $x_i$ belongs to $X$ and $y_i$ belongs to label set $Y$. This generates the weak hypothesis $h_t(i): X \rightarrow \{-1, +1\}$, as $D_t(i)$ is the weight distribution on training instance $i$ at trial $t$. The error of the hypothesis is given as

$$\varepsilon_t = Pr_{i \sim D_t}[h_t(x_i) \neq y_i] = \sum_{i:h_t(x_i) \neq y_i} D_t(i), \tag{11}$$

where the $Pr_{i \sim D_t}[.]$ is the probability with respect to the distribution $D_t(i)$ when the weak learner was trained. The parameter of weight will be chosen as

$$\alpha_t = \frac{1}{2}\ln\left(\frac{1 - \varepsilon_i}{\varepsilon_i}\right), \tag{12}$$

where $\alpha_t$ increases when $\varepsilon_t$ decreases. After updating $D_t(i)$, the final hypothesis $H$ measures the confidence in the boosting prediction, and is given as

$$H(x) = \text{sign}\left(\sum_{t=1}^{T}\alpha_t h_t(x)\right). \tag{13}$$

The final hypothesis $H$ is a majority vote in $t = 1, \ldots, T$, where $\alpha_t$ is the weight of $h_t$.

Many classifiers are constructed from a single training dataset for boosting. Each classifier is constructed to form a single decision tree structure or a rule set using the training data. New classifications are based on votes from many classifiers, while the predicted and final classes are decided from the votes. The first step of this boosting procedure is to build a single decision tree structure or a rule set from the training data. This classifier will usually contribute to the errors for some cases in the data. The first decision tree structure generates the wrong class for some cases in the training data. Next, the second classifier is constructed with greater attention to correct classification. The second classifier will consequently be different from the first classifier. The third classifier construction step is comparatively even more focused, although it also will make mistakes in some cases. By setting the boost trial number in advance, the boosting process continues iteratively by updating $D_t(i)$. The final step of the boosting process is stopped when the most recent classifier is either extremely accurate or inaccurate.

### 2.3.4. Fuzzy threshold

In a fuzzy threshold process (Quinlan, 1993, 2003), the threshold for each feature partition is divided into three ranges, including a lower bound, lb; an upper bound, ub; and a central value, $t$. If the feature value (or attribute value of the tree) in a node is below lb or above ub, the classification is partitioned using single branches corresponding to the conditions " <= " or " > ", respectively. If the feature value is between lb and ub, both branches probabilistically decide the partition results. The lower and upper bounds are calculated by approaching the apparent classification sensitivity. The fuzzy threshold can resist the effects of noise and improve the accuracy rate of classification on training and testing.

### 2.3.5. Pruning

Decision tree construction consists of two phases (Quinlan, 1986, 1993; Kirchner et al., 2006). The growth phase is generated first, followed by processing in the pruning phase. The pruning phase is used to optimize the decision tree structures. Global pruning was selected in the decision tree algorithm. Subtree replacement is performed in the pruning step when the subtree error rates for the training set are reduced. If the error rate is below the CF (25%), the nodes of the tree structure are trimmed to replace the subtree by a leaf node. The CF is the probability of a binary distribution, as defined in Eq. (14), and is calculated from the training

set. The class label of the leaf node is then defined as a simplified tree consisting of a class of attributes in a subtree. The function of pruning is to reduce the risk of overfitting the tree. Overfitting occurs when the tree is overspecialized to the training set. The pruning phase was developed to improve classification accuracy by removing subtrees that are predicted to have high error rates.

When replacing the leaf node of a tree, statistical analysis is used to obtain confidence by manipulating the posterior probability of misclassification. For example, assume an event happens $M$ times in $N$ trials. The estimated probability $p$ of the event is the ratio $M/N$. The confidence limits for $p$ can then be calculated. For the confidence CF given in Eq. (14), the estimated probability $p$ can be calculated as 1-$CF$ such that $p \leq p_r$. The upper limit $p_r$ (Diem, 1962) is satisfied as

$$CF = \begin{cases} (1 - p_r)^N, & \text{for} \quad M = 0 \\ \sum_{i=0}^{M} \binom{N}{i} p_r^i (1 - p_r)^{N-i}, & \text{for} \quad M > 0 \end{cases}, \qquad (14)$$

where CF-pruning is set to 25% as default.

### 2.4. Evaluation of segmentation

The accuracy rate was used to evaluate the performance of segmentation in the present study and was calculated based on the overlap of the standard reference image (manually labeled by an expert) and a collection of segmentation results obtained with the proposed method. The accuracy rate was quantified as the overlap fraction (Anbeek et al., 2004, 2005; He et al., 2005; Liu et al., 2005) and is defined as:

$$\text{Accuracy rate} = \frac{Ref(k) \cap Seg(k)}{Ref(k)}, \qquad (15)$$

which represents the accuracy rate of the segmented area in class $k$ relative to the area in the standard reference image (Anbeek et al., 2004, 2005). Three classes of phantom MR images (circle center, circle ring, and background) and four classes of simulated brain MR images (GM, WM, CSF, and background) were segmented in this study. The numerator in Eq. (15) represents the number of classified or intersection areas of voxels of class $k$ between the segmented image and the standard image, while the denominator represents the area of voxels in class $k$ in the standard image.

The $k$ index (also called the Dice coefficient) as given in Eq. (16), which is another means of segmentation evaluation, was also used to quantify the performance of segmentation. The $k$ index is ordinarily used to measure the similarity of two images (Dice, 1945; Marroquin et al., 2002; Archibald et al., 2003; Anbeek et al., 2004, 2005; Greenspan et al., 2006; Xia et al., 2007). Given two images, $S_1$ denotes all tissues of the standard reference image, while $S_2$ denotes all tissues of the segmented image. The $k$ index is defined as:

$$k(S_1, S_2) = \frac{2 |S_1 \cap S_2|}{|S_1| + |S_2|}, \qquad (16)$$

where $|S_1 \cap S_2|$ denotes the intersection area between $S_1$ and $S_2$. The $k$ index, running from 0 to 1, was applied to compare the segmented image and standard image (manually labeled by an expert).

### 2.5. Three-dimensional reconstruction and visualization

Each segmented image was exported separately as a distinct mat (MATLAB) file to Amira 4.1 (Mercury Computer Systems Inc., Chelmsford, MA) for surface rendered 3D models. The segmented images were first simplified using the GMC algorithm, then volume rendered with the surface rendering function in Amira. All these steps were performed with the help of the visualization and modeling software Amira (Stalling et al., 2005). The Amira User's Guide, reference manual and Amira Programmer's Guide are available at the Website http://www.amiravis.com/.

## 3. Results

### 3.1. Segmentation of SPMR images

As shown in Fig. 4, we examined the accuracy rates of SPMR image region segmentation with several levels of noise and heterogeneities (see Table 1) using various spatial features. The accuracy rates of circle center and circle ring segmentation using spatial features $(G, x, y)$, $(S, x, y)$, $(W, x, y, G, r, \theta)$, $(W, x, y, G, r, \theta, S)$, $(G, x, y, r, \theta)$, and $(S, x, y, r, \theta)$ and at different levels of noise and heterogeneity are shown in Fig. 4(a)–(b). Using the decision tree algorithm and six spatial features, the accuracy rates for circle center segmentation were greater than 0.9720, while the accuracy rates for circle ring segmentation were greater than 0.9309. The highest accuracy rate came from phantom region segmentation. The lowest accuracy rates were obtained when SPMR images were segmented using this decision tree with spatial features $(W, x, y, G, r, \theta)$ or $(W, x, y, G, r, \theta, S)$. Fig. 5 shows images segmented using this decision tree algorithm with spatial features $(G, x, y, r, \theta)$, $(S, x, y, r, \theta)$, $(W, x, y, G, r, \theta)$, and $(W, x, y, G, r, \theta, S)$ from SPMR images with noise and heterogeneity levels of Var15, Var15RF20, Var15RF40, Var30, Var30RF20, and Var30RF40. The segmentation performance was evaluated by averaging the accuracy rates of all the phantom image
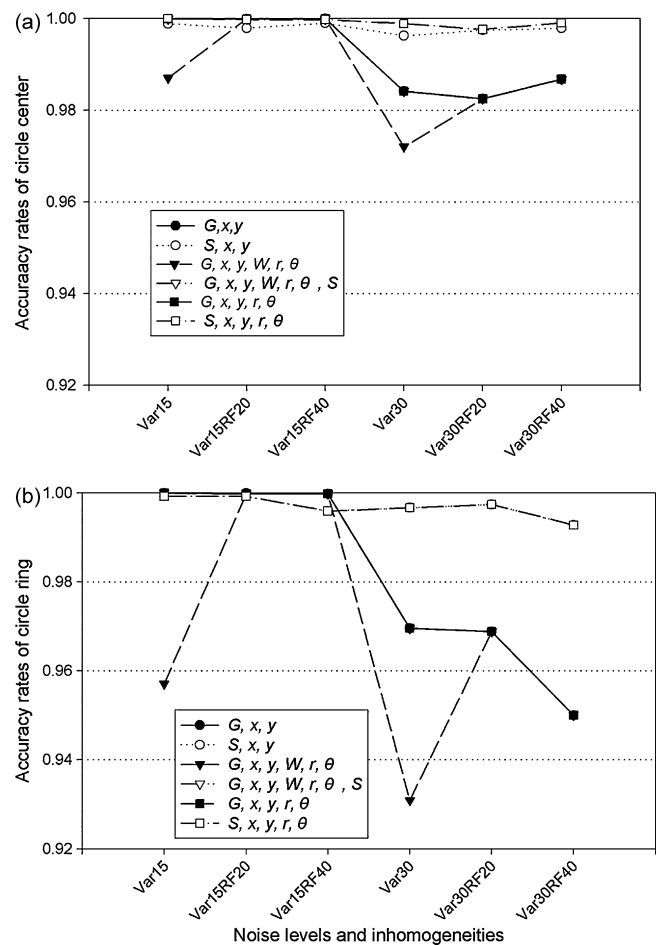


**Fig. 4.** Accuracy rates of region segmentation obtained using different spatial features from simulated phantom MR images. (a) Accuracy rates of circle center segmentation with different spatial features. (b) Accuracy rates of circle ring segmentation with different spatial features.
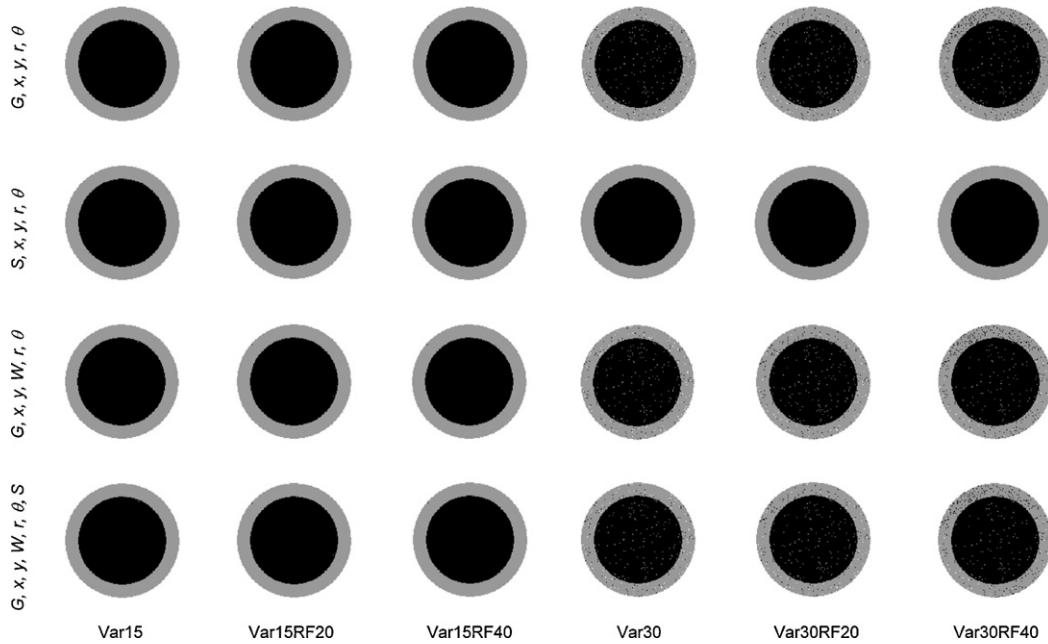
**Fig. 5.** Images segmented from simulated phantom MR images with different spatial features and various noise and heterogeneity levels.

regions in SPMR images with noise and heterogeneity levels of Var15, Var15RF20, Var15RF40, Var30, Var30RF20, and Var30RF40, and segmented with spatial features $(G, x, y, r, \theta)$, and $(S, x, y, r, \theta)$.

### 3.2. Segmentation of SBMR images

SBMR images with different noise and heterogeneity levels were segmented using the boosted decision tree algorithm with spatial features $(G, x, y)$, $(S, x, y)$, $(G, x, y, r, \theta)$, $(S, x, y, r, \theta)$, $(W, x, y, G, r, \theta)$, and $(W, x, y, G, r, \theta, S)$. Image segmentation decision tree performance was best using spatial features $(G, x, y, r, \theta)$ and $(S, x, y, r, \theta)$ in SBMR images. Fig. 6 depicts the average brain tissue segmentation accuracy using the boosted decision tree. Fig. 6(a) depicts the average segmentation accuracy using spatial feature $(G, x, y, r, \theta)$ in SBMR images with noise and heterogeneity levels of T1n7, T1n7RF20, and T1n7RF40. Fig. 6(b) depicts the average segmentation accuracy with spatial feature $(S, x, y, r, \theta)$ in SBMR images with noise and heterogeneity levels of T1n7, T1n7RF20, and T1n7RF40. Critical average accuracy rates were obtained using a decision tree with a boost trial number of 20. Greater boost trials resulted in a longer processing time. Therefore, the decision tree with 20 boost trials was selected to segment all simulated brain MR images, as shown in Fig. 6. Fig. 7(a)–(c) shows the accuracy of segmenting GM, WM, and CSF, respectively, using spatial feature $(G, x, y, r, \theta)$ on SBMR images with different noise levels and heterogeneities. The accuracy decreased for GM, WM, and CSF when segmented with spatial feature $(G, x, y, r, \theta)$ and combined with noise levels increased from 3% to 9%. Fig. 7(d)–(f) shows the accuracy of segmenting GM, WM, and CSF using spatial feature $(S, x, y, r, \theta)$ on SBMR images with different noise levels and heterogeneities. Accuracy rates decreased for GM, WM, and CSF when segmented with $(G, x, y, r, \theta)$ and including noise levels increased from 3% to 9%. Row 1 in Fig. 8 depicts a standard image (manually labeled by an expert). The images in column 1 of Fig. 8 show the original simulated brain MR images using T1n7, T1n7RF20, and T1n7RF40. The images in column 2 of Fig. 8 show simulated brain MR images segmented with spatial feature $(G, x, y, r, \theta)$ and noise and heterogeneity levels of T1n7, T1n7RF20, and T1n7RF40. The images in column 3 of Fig. 8 show SBMR images segmented with
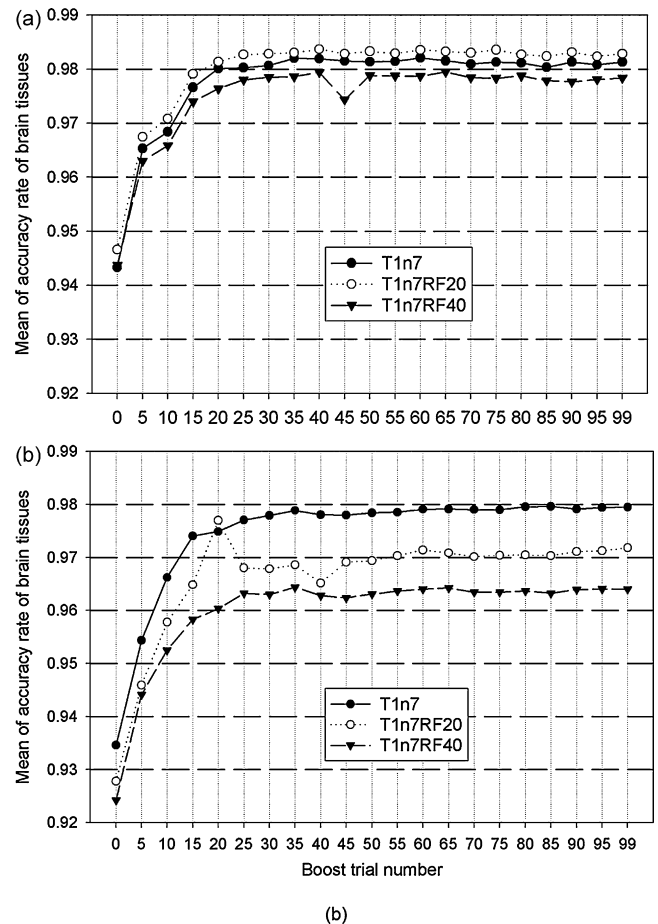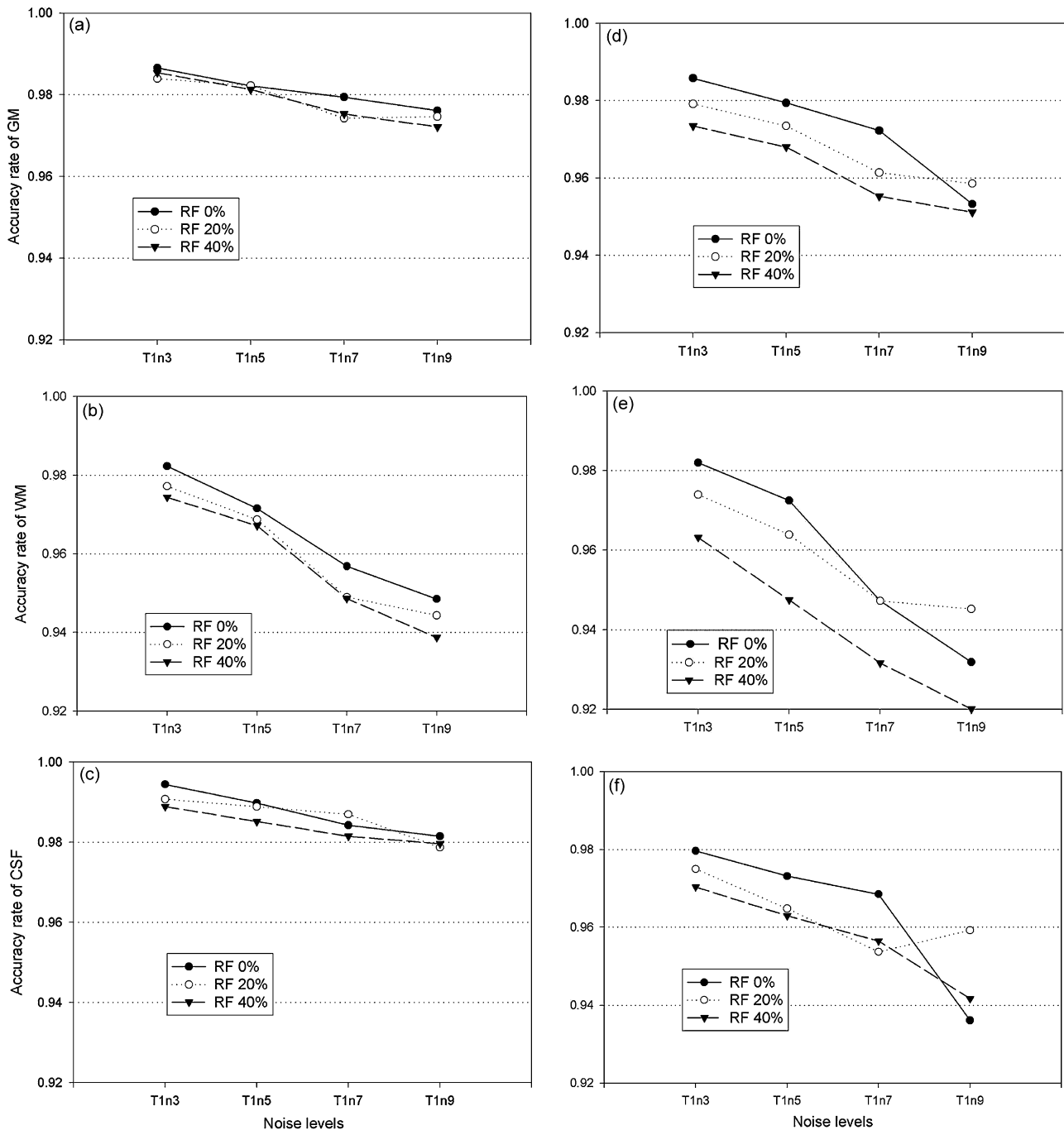


**Fig. 6.** Mean accuracy rates of tissue segmentation from simulated brain MR images. (a) Mean accuracy rates of tissue segmentation using the decision tree and 20 boost trials with spatial feature $(G, x, y, r, \theta)$ from simulated MR images with noise and heterogeneity levels T1n7, T1n7RF20, and T1n7RF40. (b) Mean accuracy rates of tissue segmentation using the decision tree combined with 20 boost trials using spatial feature $(S, x, y, r, \theta)$ from simulated MR images with noise and heterogeneity levels T1n7, T1n7RF20, and T1n7RF40.

**Fig. 7.** Accuracy rates of tissue segmentation using a boosted decision tree algorithm on simulated brain MR images. (a) Accuracy rates of GM segmentation using spatial feature ($G, x, y, r, \theta$). (b) Accuracy rates of WM segmentation using spatial feature ($G, x, y, r, \theta$). (c) Accuracy rates of CSF segmentation with spatial feature ($G, x, y, r, \theta$). (d) Accuracy rates of GM segmentation with spatial feature ($S, x, y, r, \theta$). (e) Accuracy rates of WM segmentation using spatial feature ($S, x, y, r, \theta$). (f) Accuracy rates of CSF segmentation using spatial feature ($S, x, y, r, \theta$).

spatial feature ($S, x, y, r, \theta$) and noise and heterogeneity levels of T1n7, T1n7RF20, and T1n7RF40. The boosted decision tree algorithm performed better clarity of brain tissue segmentation than that of original images. The inset images in Fig. 8 show the original and segmented SBMR images, and illustrate clear distinctions in the three brain tissues. The inset images in rows 1–3 are 3× magnifications of boxed-in locations in the original images. These three locations were difficult to segment because of their complexity. Fig. 9 shows an example of a 3D surface rendering using segmented image data, as determined by the boosted decision tree

from SBMR data with T1n7RF20, consisting of 181 slices. The brain was respectively segmented into white matter in the left hemisphere (labeled in yellow) and gray matter in the right hemisphere (labeled in orange).

### 3.3. Comparison of segmentation with the other algorithms

The results of segmentation using the boosted decision tree were also compared with another two segmentation algorithms. One is in the Medical Imaging Interaction Toolkit (MITK,
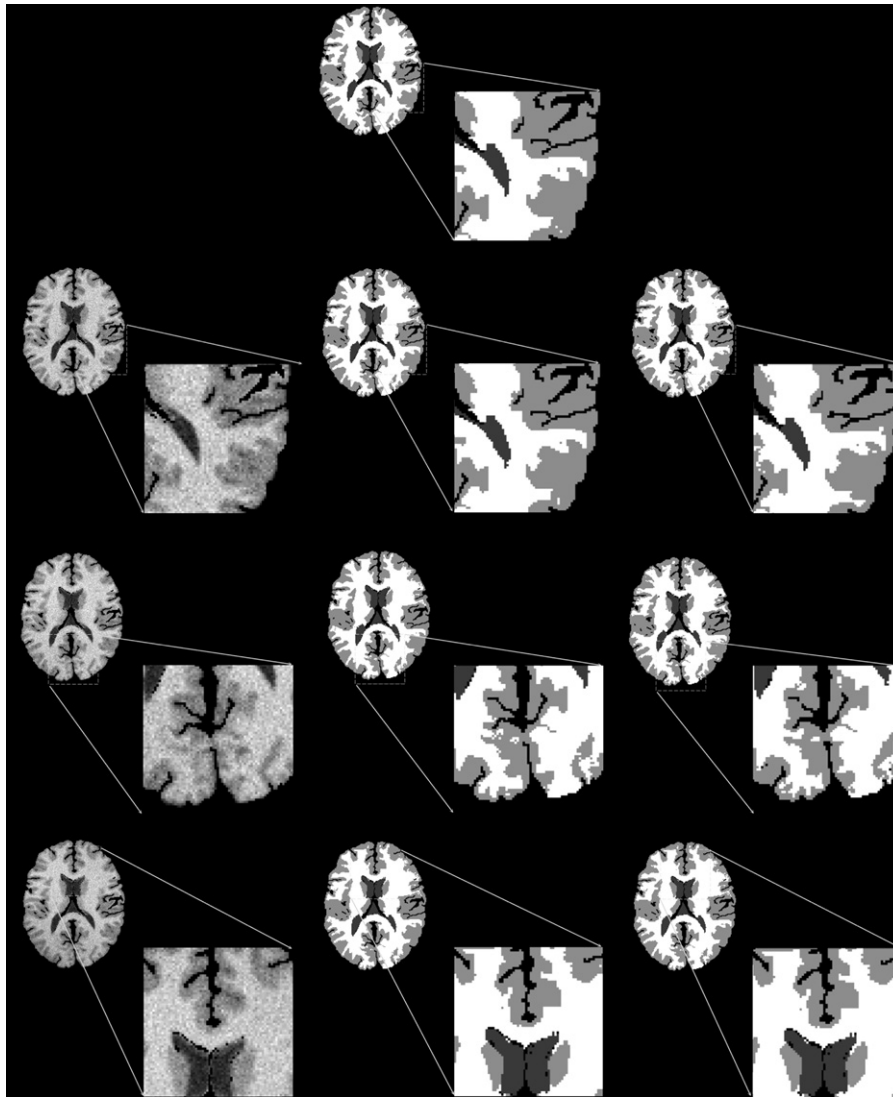
**Fig. 8.** Segmentation of simulated brain MR images from BrainWeb. Row 1 depicts the original, unsegmented image, and rows 2 through 4 show noise and heterogeneity levels T1n7, T1n7RF20, and T1n7RF40. Images in column 1 are the original images, images in column 2 are segmented with spatial feature $(G, x, y, r, \theta)$, and those in column 3 are segmented with spatial feature $(S, x, y, r, \theta)$. All blown-up images were taken from the boxed-in region of the shown whole brain horizontal slice and enlarged three times.

http://www.mitk.org/) whose principle is based on a statistical region-growing (SRG) algorithm in Insight Toolkit (ITK, http://www.itk.org/) (Wolf et al., 2005). The other is adaptive segmentation (AS) algorithm for MRI data that uses the knowledge of tissue intensity properties through the expectation maximization (EM) algorithm to more accurately segment brain MR images (Wells et al., 1996). Table 3 shows the accuracy rates of GM, WM, and CSF segmentation using the boosted decision tree with spatial features

**Table 3**
Segmentation accuracy rates from SBMR images using the boosted decision tree, the SRG, and the AS algorithm

|  | GM | | | | WM | | | | CSF | | | |
|---|---|---|---|---|---|---|---|---|---|---|---|---|
|  | $(G, x, y, r, \theta)$ | $(S, x, y, r, \theta)$ | SRG | AS | $(G, x, y, r, \theta)$ | $(S, x, y, r, \theta)$ | SRG | AS | $(G, x, y, r, \theta)$ | $(S, x, y, r, \theta)$ | SRG | AS |
| T1n3 | 0.9865 | 0.9857 | 0.6577 | 0.9349 | 0.9822 | 0.9819 | 0.9726 | 0.8329 | 0.9944 | 0.9796 | 0.6958 | 0.8148 |
| T1n5 | 0.9822 | 0.9794 | 0.7999 | 0.8873 | 0.9715 | 0.9724 | 0.9386 | 0.8576 | 0.9898 | 0.9731 | 0.7370 | 0.8250 |
| T1n7 | 0.9794 | 0.9722 | 0.9051 | 0.8254 | 0.9568 | 0.9609 | 0.8250 | 0.8325 | 0.9842 | 0.9685 | 0.7610 | 0.8407 |
| T1n9 | 0.9760 | 0.9532 | 0.9125 | 0.8099 | 0.9485 | 0.9319 | 0.5909 | 0.7033 | 0.9814 | 0.9361 | 0.7824 | 0.8407 |
| T1n3RF20 | 0.9839 | 0.9791 | 0.7448 | 0.9329 | 0.9771 | 0.9739 | 0.9636 | 0.8314 | 0.9907 | 0.9750 | 0.7169 | 0.7972 |
| T1n5RF20 | 0.9822 | 0.9734 | 0.7885 | 0.8986 | 0.9687 | 0.9638 | 0.9296 | 0.8535 | 0.9888 | 0.9648 | 0.7301 | 0.8000 |
| T1n7RF20 | 0.9742 | 0.9613 | 0.9026 | 0.8178 | 0.9490 | 0.9472 | 0.8357 | 0.8503 | 0.9870 | 0.9537 | 0.7625 | 0.8222 |
| T1n9RF20 | 0.9746 | 0.9585 | 0.9625 | 0.8182 | 0.9443 | 0.9452 | 0.3962 | 0.6364 | 0.9787 | 0.9592 | 0.7959 | 0.8463 |
| T1n3RF40 | 0.9853 | 0.9734 | 0.7761 | 0.9514 | 0.9743 | 0.9631 | 0.9471 | 0.7438 | 0.9888 | 0.9703 | 0.7112 | 0.7630 |
| T1n5RF40 | 0.9812 | 0.9679 | 0.8705 | 0.8786 | 0.9671 | 0.9474 | 0.8908 | 0.8374 | 0.9851 | 0.9629 | 0.7424 | 0.8056 |
| T1n7RF40 | 0.9753 | 0.9552 | 0.9470 | 0.8319 | 0.9486 | 0.9316 | 0.6601 | 0.7433 | 0.9814 | 0.9564 | 0.7698 | 0.8333 |
| T1n9RF40 | 0.9721 | 0.9511 | 0.9593 | 0.8077 | 0.9386 | 0.9201 | 0.4859 | 0.6591 | 0.9796 | 0.9416 | 0.7925 | 0.8333 |

**Table 4**
The segmentation $k$ indices from SBMR images using the boosted decision tree, the SRG, and the AS algorithm
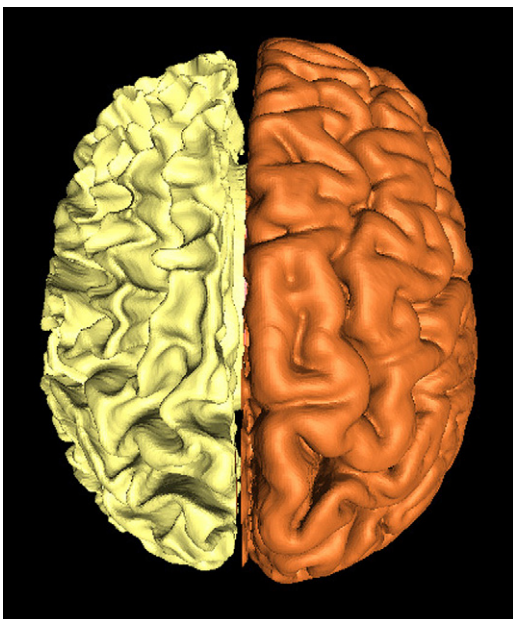
| | GM | | | | WM | | | | CSF | | | |
|---|---|---|---|---|---|---|---|---|---|---|---|---|
| | $(G, x, y, r, \theta)$ | $(S, x, y, r, \theta)$ | SRG | AS | $(G, x, y, r, \theta)$ | $(S, x, y, r, \theta)$ | SRG | AS | $(G, x, y, r, \theta)$ | $(S, x, y, r, \theta)$ | SRG | AS |
| T1n3 | 0.9839 | 0.9814 | 0.7620 | 0.8680 | 0.9850 | 0.9863 | 0.8671 | 0.8948 | 0.9898 | 0.9828 | 0.8192 | 0.7917 |
| T1n5 | 0.9757 | 0.9728 | 0.8405 | 0.8556 | 0.9775 | 0.9797 | 0.9032 | 0.8941 | 0.9861 | 0.9790 | 0.8458 | 0.7661 |
| T1n7 | 0.9663 | 0.9632 | 0.8495 | 0.8107 | 0.9683 | 0.9721 | 0.8767 | 0.8666 | 0.9815 | 0.9725 | 0.7427 | 0.7028 |
| T1n9 | 0.9602 | 0.9384 | 0.7973 | 0.7455 | 0.9624 | 0.9522 | 0.7348 | 0.7909 | 0.9774 | 0.9546 | 0.7571 | 0.6442 |
| T1n3RF20 | 0.9797 | 0.9738 | 0.8174 | 0.8654 | 0.9811 | 0.9806 | 0.8921 | 0.8921 | 0.9879 | 0.9804 | 0.8342 | 0.7863 |
| T1n5RF20 | 0.9742 | 0.9740 | 0.8357 | 0.8585 | 0.9759 | 0.9651 | 0.9072 | 0.8929 | 0.9852 | 0.9742 | 0.8408 | 0.7721 |
| T1n7RF20 | 0.9834 | 0.9503 | 0.8557 | 0.8137 | 0.9667 | 0.9628 | 0.8846 | 0.8761 | 0.9691 | 0.9662 | 0.7474 | 0.6815 |
| T1n9RF20 | 0.9572 | 0.9476 | 0.7729 | 0.7252 | 0.9594 | 0.9610 | 0.5650 | 0.7570 | 0.9759 | 0.9709 | 0.8745 | 0.5995 |
| T1n3RF40 | 0.9787 | 0.9648 | 0.8297 | 0.8332 | 0.9801 | 0.9738 | 0.8943 | 0.8404 | 0.9879 | 0.9757 | 0.8294 | 0.8000 |
| T1n5RF40 | 0.9745 | 0.9542 | 0.8613 | 0.8405 | 0.9726 | 0.9648 | 0.8963 | 0.8801 | 0.9847 | 0.9733 | 0.8498 | 0.7449 |
| T1n7RF40 | 0.9597 | 0.9390 | 0.8222 | 0.7745 | 0.9621 | 0.9544 | 0.7819 | 0.8275 | 0.9787 | 0.9672 | 0.7505 | 0.6329 |
| T1n9RF40 | 0.9528 | 0.9312 | 0.7804 | 0.7270 | 0.9554 | 0.9464 | 0.6494 | 0.7699 | 0.9769 | 0.9594 | 0.7634 | 0.5927 |

$(G, x, y, r, \theta)$ and $(S, x, y, r, \theta)$, the SRG, and the AS algorithm from SBMR images with different noise levels and heterogeneities. The accuracy rates of GM, WM, and CSF segmentation using the boosted decision tree with spatial features $(G, x, y, r, \theta)$ and $(S, x, y, r, \theta)$ at all noise levels and heterogeneities were higher than those of SRG and AS algorithm.

The $k$ index or similarity index was also used to compare segmentation performance. Table 4 summarizes the $k$ indices of segmented GM, WM, and CSF from SBMR images using the boosted decision tree with spatial features $(G, x, y, r, \theta)$ and $(S, x, y, r, \theta)$, the SRG and the AS algorithm from SBMR with different noise levels and heterogeneities. The $k$ values of segmented GM, WM, and CSF using the boosted decision tree with spatial features $(G, x, y, r, \theta)$ and $(S, x, y, r, \theta)$ were higher than 0.9312, 0.9464, and 0.9547, respectively. The $k$ indices of GM, WM, and CSF segmentation using the boosted decision tree and a fuzzy threshold were much higher than those using SRG and AS algorithm in several different noise levels and heterogeneities from SBMR images.

### 3.4. Segmentation of real data in brain MR images

The boosted decision tree, SRG, and AS algorithm were also used to segment real data from brain MR images. Two subjects (A and B)

of brain MR images were segmented for this experiment. Table 5 summarizes the results in terms of the accuracy rate and $k$ index for a real data experiment. The accuracies of GM, WM, and CSF from subject A segmented using the boosted decision tree with $(G, x, y, r, \theta)$, $(S, x, y, r, \theta)$, $(W, x, y, G, r, \theta)$, and $(W, x, y, G, r, \theta, S)$ were higher than 0.9973, 0.9979, and 0.9913, respectively. The $k$ indices of the segmented GM, WM, and CSF from subject A using the boosted decision tree with $(G, x, y, r, \theta)$, $(S, x, y, r, \theta)$, $(W, x, y, G, r, \theta)$, and $(W, x, y, G, r, \theta, S)$ were higher than 0.9942, 0.9978, and 0.9932, respectively. The accuracy rates of segmented GM, WM, and CSF from subject B using the boosted decision tree with $(G, x, y, r, \theta)$, $(S, x, y, r, \theta)$, $(W, x, y, G, r, \theta)$, and $(W, x, y, G, r, \theta, S)$ were higher than 0.9967, 0.9987, and 0.9922, respectively. The $k$ indices of segmented GM, WM, and CSF from subject B using the boosted decision tree with $(G, x, y, r, \theta)$, $(S, x, y, r, \theta)$, $(W, x, y, G, r, \theta)$, and $(W, x, y, G, r, \theta, S)$ were higher than 0.9963, 0.9984, and 0.9942, respectively. The accuracy rates and $k$ indices of segmented GM, WM, and CSF using the boosted decision tree with $(G, x, y, r, \theta)$, $(S, x, y, r, \theta)$, $(W, x, y, G, r, \theta)$, and $(W, x, y, G, r, \theta, S)$ exhibited much higher performance than those using SRG and AS segmentation algorithm from real data.

Fig. 10 depicts segmented images using the boosted decision tree and the other segmentation algorithm. Images in rows 1 and 2 of Fig. 10 were obtained from subjects A and B. Images in column



**Fig. 9.** A 3D reconstruction of segmented brain image data was shown in axial view. The brain has been segmented into gray matter (labeled in orange) and white matter (labeled in yellow).

**Table 5**
Segmentation of MR images from two real subjects using the boosted decision tree, the SRG, and the AS method

| Subject | | Spatial feature | GM | WM | CSF |
|---|---|---|---|---|---|
| Subject A | Accuracy | $(G, x, y, r, \theta)$ | 0.9974 | 0.9979 | 0.9913 |
| | | $(S, x, y, r, \theta)$ | 0.9973 | 0.9987 | 0.9897 |
| | | $(W, x, y, G, r, \theta)$ | 0.9984 | 0.9989 | 0.9968 |
| | | $(W, x, y, G, r, \theta, S)$ | 0.9982 | 0.9988 | 0.9963 |
| | | SRG | 0.7407 | 0.8624 | 0.1508 |
| | | AS | 0.6364 | 0.9169 | 0.6224 |
| | $k$ | $(G, x, y, r, \theta)$ | 0.9957 | 0.9978 | 0.9944 |
| | | $(S, x, y, r, \theta)$ | 0.9942 | 0.9979 | 0.9932 |
| | | $(W, x, y, G, r, \theta)$ | 0.9983 | 0.9987 | 0.9977 |
| | | $(W, x, y, G, r, \theta, S)$ | 0.9980 | 0.9986 | 0.9975 |
| | | SRG | 0.6735 | 0.8004 | 0.2615 |
| | | AS | 0.6889 | 0.7811 | 0.7432 |
| Subject B | Accuracy | $(G, x, y, r, \theta)$ | 0.9973 | 0.9987 | 0.9955 |
| | | $(S, x, y, r, \theta)$ | 0.9967 | 0.9988 | 0.9922 |
| | | $(W, x, y, G, r, \theta)$ | 0.9969 | 0.9992 | 0.9977 |
| | | $(W, x, y, G, r, \theta, S)$ | 0.9972 | 0.9994 | 0.9980 |
| | | SRG | 0.6635 | 0.9085 | 0.1579 |
| | | AS | 0.5432 | 0.9564 | 0.6223 |
| | $k$ | $(G, x, y, r, \theta)$ | 0.9973 | 0.9987 | 0.9966 |
| | | $(S, x, y, r, \theta)$ | 0.9963 | 0.9984 | 0.9942 |
| | | $(W, x, y, G, r, \theta)$ | 0.9984 | 0.9987 | 0.9979 |
| | | $(W, x, y, G, r, \theta, S)$ | 0.9988 | 0.9989 | 0.9982 |
| | | SRG | 0.6195 | 0.8400 | 0.2725 |
| | | AS | 0.6231 | 0.8259 | 0.7434 |
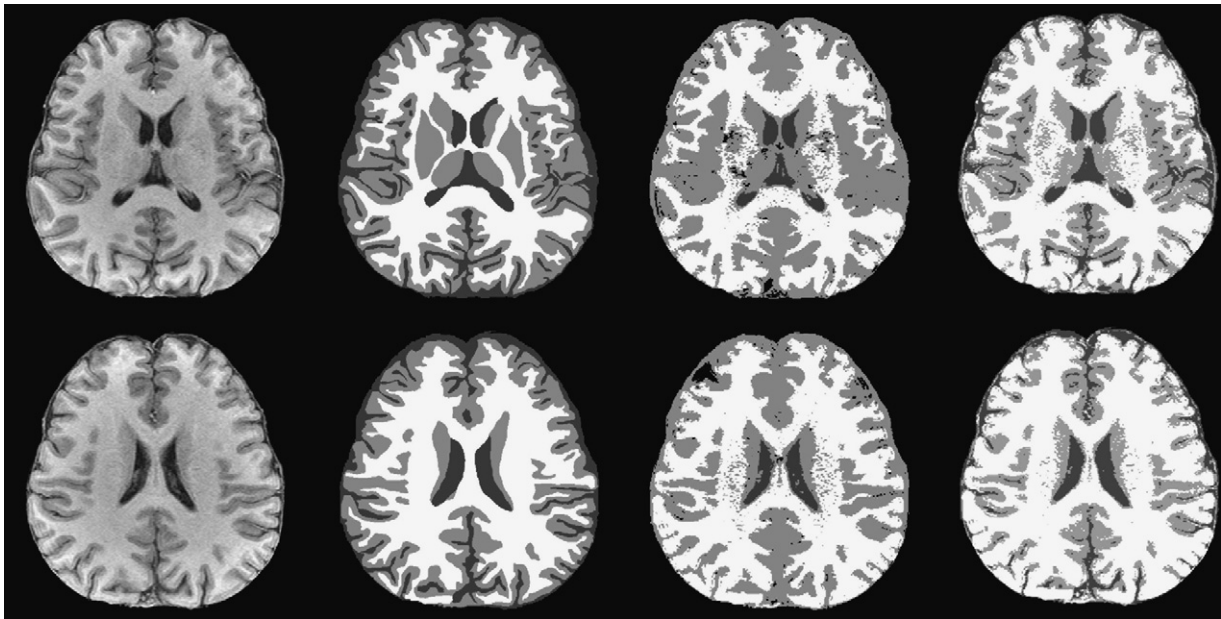
**Fig. 10.** Segmentation of real brain MR imaging data. Images in column 1 show the original brain MR images of subjects A and B. Images in column 2 correspond to those in column 1 and were segmented using the boost decision tree with spatial feature ($G, x, y, r, \theta$). Images in column 3 correspond to those in column 1 and were segmented with the SRG algorithm. Images in column 4 correspond to those in column 1 and were segmented with the AS algorithm.

1 of Fig. 10 show the original MR images from subjects A and B. Images in column 2 of Fig. 10 show images corresponding to column 1 that were segmented using the boosted decision tree with spatial features ($G, x, y, r, \theta$). Images in column 3 of Fig. 10 show images segmented with the SRG algorithm. Images in column 4 of Fig. 10 show images segmented with the AS algorithm. Clear tissue regions were identified from real segmented brain image data using the boosted decision tree, whereas unclear regions and artifacts existed in the original images and those segmented with the SRG and AS algorithm. It is, therefore, clear that visually apparent artifacts in MR images of real brains are reduced when using the boosted decision tree.

## 4. Discussion

We found better separation of intensity distributions for each region when using the decision tree than in the original SPMR images, indicating increased accuracy. Moreover, similar accuracies were found when SPMR images were segmented using decision trees with and without boost trials (data not shown). In all regions, accuracies of segmentation from SPMR images using decision tree algorithms with spatial features ($G, x, y, r, \theta$), and ($S, x, y, r, \theta$) as well as Var15, Var15RF20, Var15RF40, Var30, Var30RF20, Var30RF40 were the highest (Fig. 4). These two spatial features were, therefore, used to segment the SBMR images. The lowest accuracy rates were obtained with spatial features ($W, x, y, G, r, \theta$), and ($W, x, y, G, r, \theta, S$) because the overlapping intensity of each region was greater when spatial feature ($W$) was included (Fig. 1). Segmentation was poorest when using the decision tree algorithm on SPMR images with Var30, Var30RF20, and Var30RF40 due to larger noise variations in phantom images thus leading to increased overlap of image intensity.

The intensity distribution of each tissue in the SBMR images overlapped more and was more complex than in the SPMR images. The increased noise levels or RF heterogeneities of SBMR images often cause greater image intensity distribution overlap. The SBMR images were more difficult to correctly segment, and as such, the boosted decision tree was proposed. The accuracy rates of SBMR

tissue segmentation increased when the boost trial numbers were increased, but at the expense of a longer process, as depicted in Fig. 6. In order to limit time consumption, we elected to use 20 boost trial numbers in the decision tree algorithm to improve the accuracy of SBMR image tissue segmentation (Fig. 6). The spatial features ($G, x, y, r, \theta$) and ($S, x, y, r, \theta$) were selected as inputs to the segmentation algorithm since they provided greater accuracy when tested in SPMR images (Fig. 4). The accuracy rates of segmented brain tissues using spatial feature ($G, x, y, r, \theta$) were higher than those using spatial feature ($S, x, y, r, \theta$) since the general gray level ($G$) had less overlap in the intensity distribution for each tissue compared to the spatial gray level ($S$). The local area of spatial feature ($S$) was also larger than that of spatial feature ($G$), as shown in Fig. 1. Thus, the segmentation accuracy rates were lowest when the spatial features included wavelet transform ($W$). The segmentation accuracy rates using the boosted decision tree algorithm with spatial features ($G, x, y, r, \theta$) and ($S, x, y, r, \theta$) decreased when the noise levels in brain MR images increased (Fig. 7). The accuracy rates also decreased when the noise levels increased in conjunction with 20% or 40% RF heterogeneities. There was no significant difference in accuracy between SBMR images with 20% or 40% heterogeneity since the overlap in the intensity distribution was less affected by heterogeneities. The decrease in accuracy caused by increased noise was greater than that caused by heterogeneities.

More complicated statistical analyses or parameter adjustments are often implemented to further enhance accuracy. Several studies have examined the accuracy of MR segmentation (Marroquin et al., 2002; Archibald et al., 2003; Anbeek et al., 2005; Greenspan et al., 2006; Yu et al., 2006). Marroquin et al. (2002) studied automatic segmentation of brain MR images. Their validation was only performed on GM and WM. Archibald et al. (2003) stressed the importance of improving the accuracy evaluated by the $k$ index; however, their validation of brain MR was also limited to WM and GM. Anbeek et al. (2005) performed probability segmentation of brain tissue on MR imaging with similarity indices of 0.893 for WM, 0.830 for GM, and 0.819 for CSF. Greenspan et al. (2006) performed automatic segmentation of brain MR images from BrainWeb. The validation of segmentation was performed with maximum Dice

coefficients of 0.889 for GM, 0.920 for WM, and 0.742 for CSF on T1-weighted MR imaging with a noise level of 9%. Yu et al. (2006) segmented brain MR images from BrainWeb that had been validated with an average overlap metric (AOM) of 0.9 for WM on T1-weighted imaging with a noise level of 3% and RF of 0%. These studies addressed the importance of improving tissue segmentation accuracy in MR images. In the present study, segmentation errors were observed to decrease when the boost number was increased, while correct segmentation was not impacted by noise effects on the fuzzy threshold. The boosted decision tree algorithm combined with a fuzzy threshold performed well and accurately for SBMR image segmentation. The accuracy rates of GM, WM, and CSF segmentation using the boosted decision tree with spatial features $(G, x, y, r, \theta)$ at all noise levels and heterogeneities were higher than 0.9721, 0.9386, and 0.9787, respectively (Table 3). The highest accuracy rates were obtained when $(G, x, y, r, \theta)$ was used to classify the SBMR images. Increased boost trials provided more accurate results for SBMR imaging. Higher values of the accuracy were obtained in SBMR images when using the boosted decision tree combined with a fuzzy threshold as compared to SRG and AS for other research methods (Table 3). Thus, the boosted decision tree algorithm demonstrates improved tissue (GM, WM, and CSF) segmentation performance in SBMR images, and significantly improves the accuracy therein.

The $k$ values of segmented GM, WM, and CSF using the boosted decision tree with spatial features $(G, x, y, r, \theta)$ were higher than 0.9528, 0.9554, and 0.9769, respectively (Table 4). The $k$ index and accuracy rate were both used to evaluate the performance of the decision tree combined with boosting and a fuzzy threshold against SRG and AS algorithm. Higher values of the $k$ index were obtained using the boosted decision tree compared to using the SRG and AS algorithm (Table 4). The observed decrease of these values in the presence of increased SBMR noise was greater for the SRG and AS method than for the boosted decision tree algorithm. Noise levels and heterogeneities did not appreciably impact brain tissue segmentation using the decision tree combined with boost trials and a fuzzy threshold. As a real application, brain MR images from two subjects were segmented using the boosted decision tree, the SRG and AS algorithm. The values of the $k$ index and accuracy of segmented GM, WM, and CSF from a real data using the boosted decision tree with $(G, x, y, r, \theta)$, $(S, x, y, r, \theta)$, $(W, x, y, G, r, \theta)$, and $(W, x, y, G, r, \theta, S)$ were greater than 0.99. Higher values of the $k$ index and accuracy were produced by the boosted decision tree in comparison to the SRG and AS method on real data (Table 5). The boosted decision tree successfully segmented the tissues in MR-imaged real brains, and exhibited enhanced clarity of brain tissue (Fig. 10). Thus, the boosted decision tree algorithm is equally suitable for brain tissue (GM, WM, and CSF) segmentation in real MR images with improved accuracy.

## 5. Conclusions

The present work have demonstrated an automatic method and boosted decision tree algorithm for segmenting MR images. We presented a supervised approach to classification-created MR images, wherein structures of interest were precisely addressed by a decision tree, combined with boost trials and a fuzzy threshold.

The decision tree successfully segmented the SPMR images, and the boosted decision tree algorithm improved the accuracy of tissue segmentation from SBMR images. Furthermore, the spatial features $(G, x, y, r, \theta)$ and $(S, x, y, r, \theta)$ were used to combine the general gray level and spatial gray level with Euclidean coordinates $(x, y)$ or polar coordinates $(r, \theta)$ for image preprocessing. The highest accuracy rates and $k$ indices of brain tissue segmentation were obtained when the spatial feature $(G, x, y, r, \theta)$ was used to classify the SBMR

images. The appreciated boost trials were found to obtain more accurate results on SBMR images. The boosted decision tree algorithm also improved the accuracy of tissue segmentation from real data. Therefore, the boosted decision tree algorithm proved to be suitable for tissue (GM, WM, CSF) segmentation of brain MR images and provided improved accuracy for brain tissue segmentation.

High accuracy was shown with the proposed method as compared to other segmentation methods on the small set of processed images. However, we found the segmentation execution took approximately 15 s/slice, with our non-optimal decision tree construction and longer learning phase for image feature extraction on a 3.2 GHz Pentium Dual Core with 8GB RAM using a MATLAB® implementation of the algorithm, which is time-consuming and clinically inflexible. We are currently continuing our efforts to reduce the computation complexity of the proposed method and evaluate it with respect to computation time, degree of robustness and accuracy on a larger data set.

In this study, the RF inhomogeneity of MR images significantly decreased the accuracy rate of segmented results. Inhomogeneity resulted in pixel intensity variation across the image. Furthermore, the current method was not computationally efficient for modelling context in the image due to large data sets (181 slices of $256 \times 256 \times 16$-bit images). Hence, incorporating RF inhomogeneity correction into the proposed algorithms could greatly benefit the accuracy of the resulting segmentation.

## References

Admiraal-Behloul F, Van Den Heuvel DMJ, Van Osch OMJP, Van Der Grond J, Van Buchem MA, Reiber JHC. Fully automatic segmentation of white matter hyperintensities in MR images of the elderly. NeuroImage 2005;28:607–17.

Ali AA, Dale AM, Badea A, Johnson GA. Automatic segmentation of neuroanatomical structures in multispectral MR microscopy of the mouse brain. NeuroImage 2005;27:425–35.

Amato U, Larobina M, Antoniadis A, Alfano B. Segmentation of magnetic resonance brain images through discriminant analysis. J Neurosci Methods 2003;131:65–74.

Anbeek P, Vincken KL, Van Osch MJP, Bisschops RHC, Van Der Grond J. Probabilistic segmentation of white matter lesions in MR imaging. NeuroImage 2004;21:1037–44.

Anbeek P, Vincken KL, Van Bochove GS, Van Osch MJP, Bisschops RHC, Van Der Grond J. Probabilistic segmentation of brain tissue in MR imaging. NeuroImage 2005;27:795–804.

Andersen AH, Zhang Z, Avison MJ, Gash DM. Automated segmentation of multispectral brain MR images. J Neurosci Methods 2002;122:13–23.

Andrey P, Maurin Y. Free-D: an integrated environment for three-dimensional reconstruction from serial sections. J Neurosci Methods 2005;145:233–44.

Archibald R, Chen K, Gelb A, Renaut R. Improving tissue segmentation of human brain MRI through preprocessing by the Gegenbauer reconstruction method. NeuroImage 2003;20:489–502.

Arditi D, Pulket T. Predicting the outcome of construction litigation using boosted decision trees. J Comp Civil Eng 2005;19:387–93.

Barra V, Boire J-Y. Tissue segmentation on MR images of the brain by possibilistic clustering on a 3D wavelet representation. J Magn Reson Imag 2000;11: 267–78.

Behrens S, Laue H, Althias M, Boehler T, Kuemmerlan B, Hahn HK, et al. Computer assistance for MR based diagnosis of breast cancer: present and future challenges. Comput Med Imag Graph 2007;31:236–47.

Bittencourt HR, Clarke RT. Use of classification and regression trees (CART) to classify remotely-sensed digital images. Proc IEEE Int Geosci Remote Sens Symp 2003;6:3751–3.

Cline HE, Doumulin CL, Hart HR, Lorensen WE, Ludke S. 3-D reconstruction of the brain from magnetic resonance images using a connectivity algorithm. Magn Reson Imag 1987;5:345–52.

Dice LR. Measures of the amount of ecologic association between species. Ecology 1945;26:297–302.

Diem K, editor. Documenta Geigy Sientific Tables. Ardsley, N.Y.: Geigy Pharmaceuticals; 1962.

Dombi J, Zsiros Á. Learning multicriteria classification models from examples: decision rules in continuous space. Eur J Oper Res 2005;160:663–75.

Dou W, Ruan S, Chen Y, Bloyet D, Constans JM. A framework of fuzzy information fusion for the segmentation of brain tumor tissues on MR images. Image Vision Comput 2007;25:164–71.

Freund Y, Schapire RE. Experiments with a new boosting algorithm. In: Proceeding of the 13th international conference on Artificial Intelligence: Machine Learning. International Machine Learning Society; 1996. p. 148–56.

Freund Y, Schapire RE. A short introduction to boosting. J Jpn Soc Artif Intell 1999;14(5):148–56.

Frey L, Fisher D. Identifying Markov blankets with decision tree induction. In: Proceeding of the Third IEEE International Conference on Data Mining; 2003. p. 59–66.

Gonzalez RC, Woods RE. Digital image processing. 2nd ed. New Jersey: Prentice Hall; 2002.

Grajski KA, Breiman L, Di Prisco GV, Freeman WJ. Classification of EEG spatial patterns with a tree structured methodology: CART. IEEE Trans Biomed Eng 1986;BME-33:1076–86.

Greenspan H, Ruf A, Goldberger J. Constrained Gaussian mixture model framework for automatic segmentation of MR brain images. IEEE Trans Med Imag 2006;25:1233–45.

Gu Y, Hall LO, Goldgof D, Kanade PM, Murtagh FR. Sequence tolerant segmentation system of brain MRI. In: Proceedings of the IEEE International Conference on System, Man and Cybermetics; 2005.

Hautaniemi S, Kharait S, Iwabu A, Wells A, Lauffenburger DA. Modeling of signal-response cascades using decision tree analysis. Bioinformatics 2005;21:2027–35.

He R, Sajia BR, Narayana PA. Implementation of high-dimensional feature map for segmentation of MR images. Ann Biomed Eng 2005;33:1439–48.

Hu W, Wu O, Chen Z, Fu Z, Maybank S. Recognition of pornographic web pages by classifying texts and images. IEEE Trans Pattern Anal Mach Intell 2007;29:1019–34.

Joliot M, Majoyer BM. Three dimensional segmentation and interpolation of magnetic resonance brain images. IEEE Trans Med Imag 1993;12:269–77.

Kirchner K, Tölle KH, Krieter J. Optimization of the decision tree technique applied to simulated sow herd datasets. Comput Electron Agric 2006;50:15–24.

Liu J, Udupa JK, Odhner D, Hacney D, Moonis G. A system for brain tumor volume estimation via MR imaging and fuzzy connectedness. Comput Med Imag Graph 2005;29:21–34.

Macek J. Incremental learning of ensemble classifiers on ECG data. In: Proceedings of the 18th IEEE Symposium on Computer-Based Medical System (CBMS'05); 2005.

Marroquin JL, Vemuri BC, Botello S, Calderon F, Fernandez-Bouzas A. An accurate and efficient Bayesian method for automatic segmentation of brain MRI. IEEE Trans Med Imag 2002;21:934–45.

Mohr J, Hess A, Scholz M, Obermayer K. A method for automatic segmentation of autoradiographic image stacks and spatial normalization of functional cortical activity patterns. J Neurosci Methods 2004;134:45–58.

Noulhiane M, Samson S, Clemenceau S, Dormont D, Baulac B, Hasboun D. A volumetric MRI study of the hippocampus and the parahippocampal region after unilaterial medial temporal lobe resection. J Neurosci Methods 2006;156:293–304.

Quinlan JR. Induction of decision tree. Mach Learn 1986;1:81–106.

Quinlan JR. C4. 5: programs for machine learning. San Mateo, CA: Morgan Kaufmann; 1993.

Quinlan JR. Improved use of continuous attributes in C4.5. J Artif Intell Res 1996;4:77–90.

Quinlan JR. Data mining tools See5 and C5.0. Austria: RuleQuest Research, http://www.rulequest.com/see5-info.html, 2003.

Ranilla J, Luaces O, Bahamonde A. A heuristic for learning decision trees and pruning them into classification rules. AI Commun 2003;16:71–87.

Rettmann ME, Han X, Xu C, Prince JL. Automatic sulcal segmentation using watersheds on the cortical surface. NeuroImage 2002;15:329–44.

Schiemann T, Tiede U, Hohne KH. Segmentation of visible human for high quality volume-based visualization. Med Imag Anal 1996;1:263–70.

Shan ZY, Ji Q, Gajjar A, Reddick E. A knowledge-guided active contour method of segmentation of cerebella on MR images of pediatric patients with medulloblastoma. Magn Reson Imag 2005;21:1–11.

Shiue YR, Guh RS. The optimization of attribute selection in decision tree-based production control systems. Int J Adv Manuf Technol 2006;28:737–46.

Stalling D, Westerhoff M, Hege HC. Amira – an object oriented system for visual data analysis. In: Johnson CR, Hansen CD, editors. Visualization handbook. Academic Press; 2005.

Tang H, Wu EX, Ma YQ, Gallagher D, Perera GM, Zhuang T. MRI brain image segmentation by multi-resolution edge detection and region selection. Comput Med Imag Graph 2000;24:349–57.

Wells WM, Grimson WEL, Kikinis R, Jolesz FA. Adaptive segmentation of MRI data. IEEE Trans Med Imag 1996;15:429–42.

Wolf I, Vetter M, Wegner I, Böttger T, Nolden M, Schöbinger M, et al. The medical imaging interaction toolkit. Med Imag Anal 2005;9:594–604.

Xia Y, Bettinger K, Shen L, Reiss AL. Automatic segmentation of the caudate nucleus from human brain MR images. IEEE Trans Med Imag 2007;26:509–17.

Xue Z, Shen D, Davatzikos C. Determining correspondence in 3-D MR brain images using attribute vectors as morphological signatures of voxels. IEEE Trans Med Imag 2004;23:1276–91.

Yoo S-S, Lee C-U, Choi BG, Saiviroonporn P. Interactive 3-dimensional segmentation of MRI data in personal computer environment. J Neurosci Methods 2001;112:75–82.

Yu ZQ, Zhu Y, Yang J, Zhu YM. A hybrid region-boundary model for cerebral cortical segmentation in MRI. Comput Med Imag Graph 2006;30:197–208.

Zhou LQ, Zhu YM, Bergot C, Laval-Jeantet AM, Bousson V, Laredo JD, et al. A method of radio-frequency inhomogeneity for brain tissue segmentation in MRI. Comput Med Imag Graph 2001;25:379–89.

Zoroofi RA, Nishii T, Sato Y, Sugano N, Yoshikawa H, Tamura S. Segmentation of avascular necrosis of the femoral head using 3D MR images. Comput Med Imag Graph 2001;25:511–21.

Zoroofi RA, Sato Y, Nishii T, Sugano N, Yoshikawa H, Tamura S. Automated segmentation of necrotic femoral head from 3D MR data. Comput Med Imag Graph 2004;28:267–78.